MODELLING ROUGHNESS AND RECEPTIVITY IN THREE-DIMENSIONAL BOUNDARY LAYERS

David Tempelmann[1,*], Lars-Uve Schrader[1], Ardeshir Hanifi[1,2], Luca Brandt[1], Dan Henningson[1]

[1]Linné FLOW Centre, SeRC, KTH Mechanics, SE-100 44 Stockholm, Sweden
[2]Swedish Defence Research Agency, FOI, SE-164 90 Stockholm, Sweden

ABSTRACT

The receptivity of a swept-wing boundary layer to localised surface roughness is studied by means of direct numerical simulations (DNS). The flow case considered is meant to model wind tunnel experiments performed at the Arizona State University by Saric & coworkers. The receptivity amplitude of the crossflow disturbances predicted by the DNS is 40% of that measured in the experiments. The DNS results are then used to evaluate the performance of different receptivity models based on either the parabolised stability equations or the finite Reynolds number theory (FRNT). In general it is found that receptivity amplitudes are well predicted for micron sized roughness elements if non-parallel effects are accounted for.

INTRODUCTION

Receptivity models describe how an external disturbance environment is filtered by the boundary layer. Free-stream turbulence, acoustic noise or surface roughness represent the most common external disturbances.

The receptivity process is often neglected in transition prediction models. However, it has been shown in experiments by Saric & coworkers and by Bippes (1999) that the transition scenario in three-dimensional boundary layers strongly depends on the external disturbance environment. In environments exhibiting high levels of freestream turbulence unsteady boundary layer disturbances dominate over stationary disturbances excited by surface roughness. Conversely, in low-level turbulence environments, such as free flight, stationary disturbances dominate. Hence, robust transition models should account for receptivity.

In this study we focus on the excitation of crossflow disturbances by localised surface roughness. The case considered is a swept-wing boundary layer which has been studied experimentally by Saric & coworkers (see e.g. Reibert *et al.* (1996); Saric *et al.* (1998)). Several attempts to model these experiments both numerically and theoretically have been made. Ng & Crouch (1999) modelled the receptivity using finite Reynolds number theory which is based on the parallel flow assumption and obtained receptivity amplitudes close to the experimental ones. Haynes & Reed (2000) were able to correctly predict the nonlinear disturbance evolution by solving the nonlinear parabolised stability equations (NPSE). However, they did not model receptivity but extracted initial amplitudes from experimental data. Nishino & Shariff (2009) performed a DNS but obtained receptivity amplitudes far below those measured in the experiments and suspected their roughness model to be inadequate.

The aim of this study is to carefully compare different approaches of modelling boundary layer receptivity to surface roughness. We use both direct numerical simulations and parabolised stability equations (PSE). The latter may be used in combination with their respective adjoint (APSE) to predict receptivity. Further, we compare to the FRNT results by Ng & Crouch (1999).

FLOW CONFIGURATION

In the following we examine the flow over a swept wing (NLF(2)-0415 airfoil Somers & Horstmann (1985)) mounted in a wind tunnel. In order to obtain a strong negative pressure gradient on the upper wing side and thus a strong crossflow instability Reibert *et al.* (1996) chose a sweep angle of $\phi_0 = 45^\circ$ and an angle of attack of $\alpha_a = -4^\circ$. The Reynolds number was $Re_c = U_\infty c/\nu = 1.2 \times 10^6$ where U_∞ denotes the streamwise velocity of the incoming freestream, c represents the unswept chord of the wing and ν is the kinematic viscosity. The airfoil and the adopted coordinate systems are shown in figure 1. Here, (x,y,z) denote chordwise, normal and spanwise directions while (U,V,W) represent the respective velocity components. Curvilinear coordinates are defined as (ξ,η,z) which define tangential, wall-normal and spanwise directions. The corresponding velocity components will be denoted as (U_ξ, V_η, W).

DIRECT NUMERICAL SIMULATIONS

The spectral element method (SEM) has been used to perform direct numerical simulations of the flow case described in the previous section. The SEM which was introduced by Patera (1984) provides spectral accuracy in space while allowing for the geometrical flexibility of finite element methods. We use the NEK5000 simulation code developed by Fischer *et al.* (2008).

The spatial discretisation is obtained by decomposing the physical domain into spectral elements which in turn are subdivided into arrays of Gauss-Lobatto-Legendre (GLL) nodes

*email: david@mech.kth.se

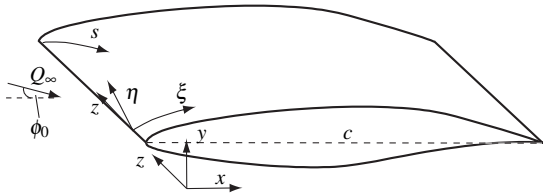

Figure 1. Swept NLF(2)-415 wing, with sweep angleϕ_0 and the total incoming velocity Q_∞. (ξ,η,z) and (x,y,z) represent curvilinear and cartesian coordinate systems respectively while s denotes the direction parallel to the incoming freestream which is tangential to the wing surface.

for the velocity and Gauss-Legendre (GL) nodes for the pressure field. The solution to the Navier-Stokes equations is approximated element-wise as a sum of Legendre polynomials up to order N, forming an orthogonal basis. The following results have been obtained using $N = 11$ for the velocity grids and $N = 9$ for the pressure grids. The staggered pressure grid makes the specification of pressure boundary conditions unnecessary. This choice is referred to as a $\mathbb{P}_N - \mathbb{P}_{N-2}$ discretisation (Maday & Patera (1989)). The present SEM code was optimized for MPI based usage on supercomputers with thousands of processors by Tufo & Fischer (2001). Here, we performed parallel computations on either 512 or 1024 processors.

Baseflow

Direct numerical simulations (DNS) of the flow over the swept-wing including the wind tunnel test section are not feasible despite the highly parallelised and optimised SEM code. The approach chosen for the current study is to perform RANS simulations of the whole wind tunnel test section. The RANS are solved using the EDGE code developed at FOI (Eliasson (2002)). The resulting flow field can be seen in figure 2. Direct numerical simulations have then been performed for the two additional domains sketched in figure 2 by prescribing no-slip, zero-stress and periodic boundary conditions at the wall, the outflow and the lateral boundaries respectively. At the inflow and top boundaries of domain 1 the velocities extracted from the RANS solution have been prescribed as Dirichlet conditions. Accordingly, Dirichlet conditions are extracted from the DNS of domain 1 and prescribed at the freestream and inflow boundary of domain 2.

All DNS results presented in this paper have been obtained for domain 2. Domain 1 has been used in a previous study by Schrader *et al.* (see Schrader (2010)) and serves here to provide correct boundary conditions for domain 2. Domain 1 includes parts of the flow over the lower side of the wing in order to account for the asymmetry of the flow configuration. It turned out that the flow separated from the lower wing surface slightly downstream of the leading edge. This separation was also observed by Nishino & Shariff (2010). The vortex shedding caused by the separation led to a local backflow at the lower outlet, destabilizing the simulations. Numerical tests revealed that the separation bubble had a negligible effect on the flow field of the upper wing side. We therefore eliminated the separation by using a sponge region, in which the flow was forced towards the time average of the separation bubble.

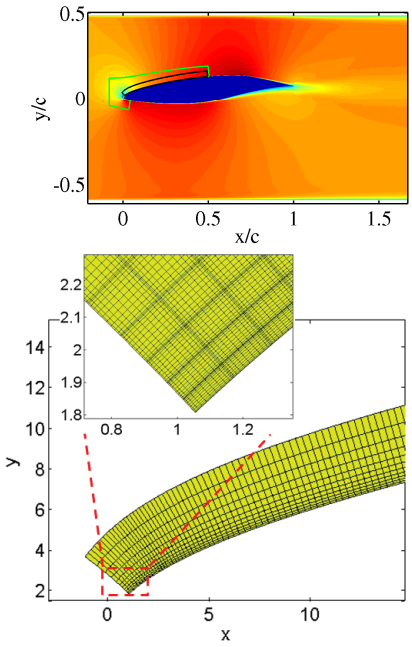

Figure 2. (a) Excerpt of the velocity field obtained from a RANS solution of the whole set-up including the wind tunnel test section. Domain 1 (green box) and domain 2 (black box) have been used for DNS of the current set-up. (b) Computational mesh for domain 2.

The computational mesh used to discretise domain 2 is presented in figure 2 (b). Both DNS meshes have been generated using the *gridgen-c* code by Sakov (2011) which represents an implementation of the Schwartz-Christoffel transformation and thus provides quasi-orthogonal grids.

The baseflow (flow field without roughness) is validated by comparing to experimental results as well as to corresponding solutions of the boundary layer equations. The pressure coefficient obtained using domain 1 ('short box') lies slightly below that of Haynes & Reed (2000) (see figure 3). An additional computation using a longer box yielded a pressure coefficient which is in excellent agreement with the result by Haynes & Reed (2000). This indicates a certain upstream-flow sensitivity to outflow conditions. However, auxiliary PSE calculations revealed that the disturbance evolution is unaffected by the slight difference of the pressure gradient. We have therefore decided to use the short (cheap) DNS box for the receptivity study. The pressure coefficient extracted from the DNS is used to solve the quasi-three-dimensional boundary layer equations (BLE) starting with the stagnation point solution. Curvature effects are neglected when solving the BLE. Figure 4 compares displacement thickness δ^*, momentum loss thickness Θ as well as boundary layer profiles of U_ξ obtained from both the DNS and BLE. Overall we obtain a very good agreement especially for positions further downstream. This is expected since the assumption of slow variation in the ξ-direction which is essential to the BLE is questionable close to the stagnation point.

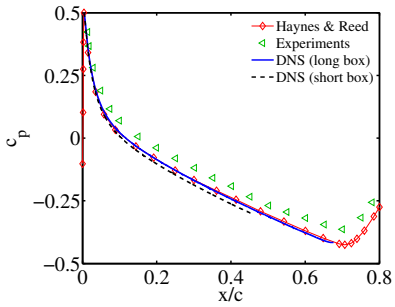

Figure 3. Comparison of computed and experimental pressure coefficients at the upper wing side.

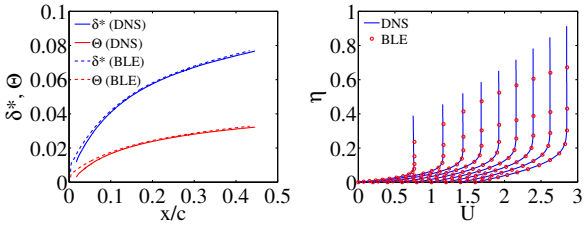

Figure 4. Comparison of displacement and momentum loss thickness (left) and profiles U_ξ (right) obtained from the DNS and the BLE solution. Note that the profiles U_ξ are shifted according to $U_{\xi,k} = U_\xi + 0.2k$ where $k = 1,2,\cdots,8$ changing from the leftmost to the rightmost profile in (b).

Roughness Modelling

The next step is to introduce the surface roughness into the DNS. In the following we consider the cylindrical roughness elements used by Reibert *et al.* (1996) (spacing $L = 12mm$, diameter $d = 3.7mm$, height $h = 6\mu m$, roughness position $x_r/c = 0.023$). The fundamental mode excited by this roughness array has a spanwise wavenumber $\beta_0 = 2\pi/L$ and represents the naturally most unstable steady crossflow disturbance. We follow two approaches. The first one is to mesh the physical wing geometry including the cylindrical roughness element. However, this is not necessarily straightforward. Many DNS codes do not allow to mesh roughness elements with heights of the order of 1% of the boundary layer thickness. Also, many simplified methods, e.g. the parabolised stability equations described later, are not capable of meshing a roughness element. In such cases a different approach is commonly used which builds on representing the roughness elements by inhomogeneous boundary conditions along the wall. The SEM method enables us to consider both approaches and to compare their performance. Figure 5 shows parts of the meshed wall including the roughness element. The roughness model is implemented by projecting the no-slip boundary conditions at the roughness to the undisturbed wall using Taylor series expansions. Hence, the wall boundary conditions become

$$u_{i,w} = -(x_r - x_w)\frac{\partial U_i}{\partial x}\bigg|_{x_w,y_w} - (y_r - y_w)\frac{\partial U_i}{\partial y}\bigg|_{x_w,y_w} + \cdots (1)$$

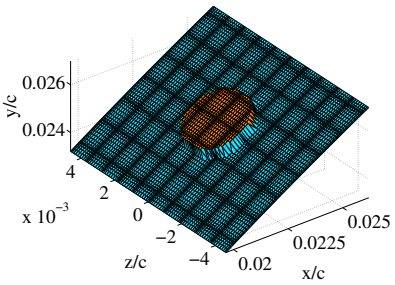

Figure 5. Meshed cylindrical roughness element generated by displacing the GLL points. For visualisation purposes the height is scaled by a factor of 100.

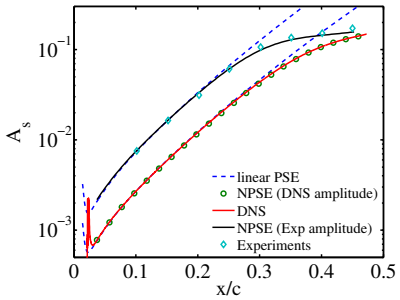

Figure 6. Disturbance amplitudes obtained from the current DNS and those measured in the experiments. The NPSE results shown have been initiated based on the respective DNS/experimenta data.

where lowercase and uppercase letters denote disturbance and baseflow quantities respectively. The subscript i represents velocity components (u,v,w) and the subscripts r and w represent coordinates of the rough and the undisturbed wall respectively. When the roughness model is used we solve the linearised Navier-Stokes equations (LNS). The steady baseflow needed for such a *linear* DNS is that presented in the previous section.

Results

Figure 6 presents amplitudes of the fundamental mode extracted from both the experiments and the DNS (meshed roughness). Note that we define disturbance amplitudes A_s as

$$A_s = \max_\eta \frac{\hat{u}_s}{U_s}, \qquad (2)$$

where '$\hat{}$' represents spatial rms values and the subscript s denotes velocity components in the wind tunnel plane which are tangential to the wing surface (see figure 1). It is apparent that the disturbance amplitudes predicted by the DNS are lower than those extracted from the experiments by Reibert *et al.* (1996). In the region of linear disturbance growth the DNS solution exhibits amplitudes which are 40% of the experimental ones. A comparison of the DNS result to linear PSE shows that nonlinear effects become apparent at 31% chord as

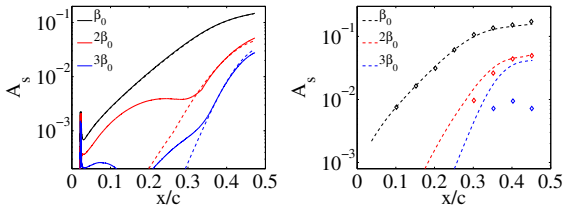

Figure 7. Disturbance amplitudes of the fundamental mode and two superharmonics obtained from DNS (—) and experiments (◇) compared to the respective NPSE results (---).

opposed to the experimental measurements where saturation sets in at about 23% chord. However, the initial linear disturbance growth predicted by the DNS is in excellent agreement to experimental observations as can be seen by comparing to the corresponding linear PSE curves. A nonlinear PSE calculation has been performed by initiating the fundamental mode ($\beta_0 = 2\pi/L$) with the amplitude extracted from the DNS field at 10% chord. The NPSE prediction matches the DNS amplitude perfectly. Even the amplitudes of the first two superharmonics ($2\beta_0, 3\beta_0$) match well in the region of modal growth (see figure 7a). The non-modal growth apparent in the DNS solution which represents the evolution of several superposed disturbances of different chordwise wavenumbers α excited by the roughness element are not predicted by the NPSE. If the initial amplitude extracted from the DNS is multiplied by a factor of 2.6 the NPSE prediction perfectly reproduces the amplitude evolution experienced in the experiments. This would correspond to choosing a roughness height of $15.6\mu m$ in the DNS. Also here, the amplitude of the first superharmonic $2\beta_0$ is predicted well. The discrepancy concerning the second superharmonic $3\beta_0$ might be due to the difficulty to accurately extract such low amplitudes from experimental measurements.

Direct numerical simulations of the LNS have been performed for four different roughness heights ($h = 6\mu m$, $2h$, $10h$, $20h$). The roughness has been modelled according to (1). The results are compared to nonlinear DNS where the roughness elements have been meshed. The resulting receptivity amplitudes at the roughness position x_r are shown in figure 8. A comparison between linear and nonlinear DNS results shows that the linear model is able to reproduce disturbance amplitude for micron-sized roughness elements of heights which are less than about 8% of the boundary layer thickness.

PARABOLISED STABILITY EQUATIONS

The parabolised stability equations first proposed by Herbert & Bertolotti (see e.g. Herbert (1997)) have been widely used to predict the linear and nonlinear evolution of disturbances in convectively unstable flows. Although both the linear and the nonlinear PSE have been employed here to predict the disturbance growth we will give a brief introduction to the linear PSE in the following since they are used to predict the receptivity. More information about the nonlinear PSE can be found in Bertolotti *et al.* (1992). The linear PSE

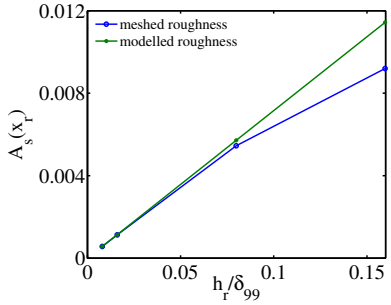

Figure 8. Receptivity amplitudes A_s of the fundamental crossflow modes at the roughness location obtained from nonlinear DNS with meshed roughness and from solving the LNS using the linear roughness model. $A_s(x_r)$ is obtained by projecting the mode amplitude to the roughness position x_r using the respective PSE solution.

build on assuming disturbances of the form

$$\mathbf{q}'(\xi,\eta,z,t) = \mathbf{q}(\xi,\eta)\Theta(\xi)\exp i(\beta z - \omega t) \qquad (3)$$

where $\Theta(\xi) = \exp i\left(\int_{\xi_0}^{\xi} \alpha(\xi')d\xi'\right)$, $\mathbf{q} = (u_\xi, v_\eta, w, p)^T$ and (ξ,η,z) represent orthogonal curvilinear coordinates (see figure 1). The corresponding tangential and spanwise wavenumbers are (α,β) while the angular frequency and time are denoted by ω and t. In the following we use $\hat{\mathbf{q}}(\xi,\eta) = \mathbf{q}(\xi,\eta)\Theta(\xi)$. Introducing ansatz (3) into the LNS and assuming a slow variation of $\mathbf{q}$ in the ξ-direction some terms including the second derivatives with respect to ξ can be neglected yielding a nearly parabolic system of equations of the form

$$\mathbf{A}\mathbf{q} + \mathbf{B}\frac{\partial \mathbf{q}}{\partial \eta} + \mathbf{C}\frac{\partial^2 \mathbf{q}}{\partial \eta^2} + \mathbf{D}\frac{1}{h_1}\frac{\partial \mathbf{q}}{\partial \xi} = 0. \qquad (4)$$

with **A**, **B**, **C** and **D** being linear operators. The scaling factor that arises due to the orthogonal curvilinear metric is given by $h_1^2 = \sum_{j=1}^{3}(\partial x_j/\partial\xi)^2$ where x_i represents the cartesian coordinates of the reference system.
Since both $\mathbf{q}$ and α in ansatz (3) are functions of ξ an auxiliary condition of the form $\int_0^\infty \mathbf{q}^H \frac{\partial \mathbf{q}}{\partial \xi}\, d\eta = 0$ is introduced ensuring both the growth and periodic variations of the disturbance to be absorbed by the exponential part of equation (3). The coupled nonlinear system of (4) and the auxiliary condition is solved iteratively while the Dirichlet boundary conditions $(u_\xi, v_\eta, w) = 0$ are imposed in the freestream and at the smooth wall.

Receptivity

The use of adjoint solutions to predict the receptivity of boundary layers was introduced by Hill (1995, 1997). He notes that adjoint eigensolutions act as a filter on a general disturbance field enabling to identify the amplitude of the corresponding eigenmode. The adjoint PSE derived in the following thus enable us to determine the receptivity amplitudes

of disturbances excited by surface roughness.
The adjoint PSE are defined by constructing a Lagrange identity of the form

$$< \mathbf{q}^*, \mathscr{L}\mathbf{q} >=< \mathscr{L}^*\mathbf{q}^*, \mathbf{q} > +\nabla \cdot \mathscr{J}(\mathbf{q}, \mathbf{q}^*), \tag{5}$$

where $\mathscr{L}$ is a linear operator representing equation (4), $\mathscr{J}$ is the so-called *bilinear concomitant* and '$*$' denotes adjoint quantities. The adjoint state vector is defined as $\mathbf{q}^* = (p^*, u^*_\xi, v^*_\eta, w^*)^T$. The inner product is defined according to $< \mathbf{a}, \mathbf{b} >= \int\int_\Omega \mathbf{a}^H \mathbf{b} h_1 \, d\xi \, d\eta$ for some $\mathbb{C}^n$-valued functions $\mathbf{a}$ and $\mathbf{b}$ and $\Omega = [\xi_0, \xi_1] \times [0, \infty]$. The superscript H denotes conjugate transpose. $\mathscr{L}^*\mathbf{q}^* = 0$ are the adjoint PSE (for a derivation see e.g. Tempelmann *et al.* (2010)). By imposing Dirichlet boundary conditions $(u^*_\xi, v^*_\eta, w^*) = 0$ in the freestream and at the wall the last term in (5) becomes

$$\begin{aligned} &\int_0^\infty \left[(\mathbf{q}^*)^H \mathbf{D}\mathbf{q} \right]_{\xi_0}^{\xi_1} d\eta = \\ &- \int_{\xi_0}^{\xi_1} \left[(\mathbf{q}^*)^H \mathbf{B}\mathbf{q} h_1 - \left(\frac{\partial \mathbf{q}^*}{\partial \eta} \right)^H \mathbf{C}\mathbf{q} h_1 \right]_{\eta=0} d\xi \end{aligned} \tag{6}$$

Now we introduce $J(\xi) = \int_0^\infty (\mathbf{q}^*)^H \mathbf{D}\tilde{\mathbf{q}} d\eta$ as well as an amplitude $A_s = \max_\eta |\hat{u}_s|$ such that $\mathbf{q} = \Theta^{-1} A_s \tilde{\mathbf{q}}$ with $\tilde{\mathbf{q}}$ being the normalised state vector. It follows that

$$\Theta^{-1} A_s J = \int_0^\infty (\mathbf{q}^*)^H \mathbf{D}\mathbf{q} \, d\eta. \tag{7}$$

Further, we assume that inhomogeneous boundary conditions do not affect the shape but just the amplitude of $\mathbf{q}'$ and that $A(\xi_0) = 0$. The surface roughness is modelled as inhomogeneous boundary conditions of the form

$$\hat{u}_{\xi,w}(\xi) = -\frac{\partial U_\xi}{\partial \eta}\bigg|_{\eta=0} H_\beta(\xi) \tag{8a}$$

$$\hat{v}_{\eta,w}(\xi) = 0 \tag{8b}$$

$$\hat{w}_w(\xi) = -\frac{\partial W}{\partial \eta}\bigg|_{\eta=0} H_\beta(\xi) \tag{8c}$$

yielding a roughness model identical to (1). The roughness is represented as discrete Fourier modes $H_\beta(\xi)$ in the spanwise direction. With $\mathbf{q} = \Theta^{-1}\hat{\mathbf{q}}$ we can insert (8) into (6). Further substituting (7) into (6) yields the receptivity amplitude as

$$\begin{aligned} A_s(\xi_1) = &\frac{1}{J(\xi_1) Re} \int_{\xi_0}^{\xi_1} \exp\left(i \int_\xi^{\xi_1} \alpha(\xi') \, d\xi' \right) \\ &\times H_\beta(\xi) \left[\frac{\partial \bar{u}^*_\xi}{\partial \eta} \frac{\partial U_\xi}{\partial \eta} h_1 + \frac{\partial \bar{w}^*}{\partial \eta} \frac{\partial W}{\partial \eta} h_1 \right]_{\eta=0} d\xi, \end{aligned} \tag{9}$$

with (ξ_0, ξ_1) being some arbitrary positions upstream and downstream of the roughness element respectively. J is evaluated for the undisturbed, homogeneous case. Hence, the receptivity is evaluated from the adjoint variables and the shear at the wall. This allows us to extract receptivity amplitudes for arbitrary roughness positions from one solution of the direct and adjoint PSE for the crossflow mode of interest.
Note that for roughness positions close to the stagnation point the receptivity amplitudes predicted by the PSE model are sensitive to the initial location ξ_0. This is due to the fact that the PSE are initiated with a local Orr-Sommerfeld mode which, when integrated downstream, is subject to a transient adjustment to the non-parallel boundary layer.

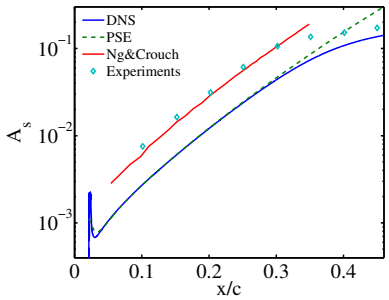

Figure 9. Comparison between the PSE model, the local model by Ng & Crouch (1999) and data from DNS and experiments.

Results

Figure 9 compares the disturbance amplitudes predicted by two receptivity models to those obtained from experiments and DNS for the roughness position considered in the experiments. The receptivity models considered are the above described PSE model and the FRNT which is based on the assumption of locally parallel flow. The latter model has been applied to the current case by Ng & Crouch (1999) and we compare to their results. The amplitudes predicted by the PSE model are slightly higher (about 3%) than those obtained from the DNS. On the other hand, the amplitudes predicted by Ng & Crouch (1999) based on FRNT are more than a factor of 2 higher and thus closely match those measured in the experiment. This is not a contradiction though. It is well known that receptivity models based on the assumption of a locally parallel baseflow overpredict disturbance amplitudes. Neglecting surface curvature as was done by Ng & Crouch (1999) just has a small increasing effect on the receptivity amplitude in this case and thus does not counteract the amplitude reduction due to the parallel flow assumption. Hence, the results obtained by Ng & Crouch (1999) are consistent with our DNS and PSE.
As explained above we can obtain the receptivity to localised surface roughness at different roughness positions from one PSE and one adjoint PSE solution only. We then evaluate the integral expression (9) for different functions $H_\beta(\xi)$. The result is shown in figure 10 where the roughness position is represented by x_r and the receptivity amplitude is given as the respective disturbance amplitude A_s at the position of neutral stability. The agreement between the PSE prediction and DNS results for different roughness positions is almost perfect. For increasing roughness positions receptivity is monotonically decreasing and hence, maximum receptivity is found upstream of branch 1 which is in correspondence to the results by Ng & Crouch (1999).

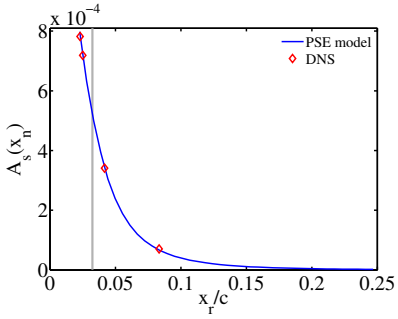

Figure 10. Disturbance amplitude $A_s(x_n)$ at the neutral point versus the roughness position x_r. The grey vertical line denotes the position of the neutral point.

CONCLUSIONS

The receptivity of a swept-wing boundary layer to localised cylindrical roughness elements has been studied by performing direct numerical simulations. The surface roughness has been introduced into the computational mesh as well as modelled based on inhomogeneous boundary conditions. We find disturbance amplitudes which are about 40 % and thus of the same order as those measured in corresponding experiments by Reibert *et al.* (1996). Results obtained with a roughness model based on projecting no-slip conditions to the undisturbed wall agree perfectly to the results obtained with the meshed roughness until roughness heights exceed 8% of the boundary layer thickness. We further evaluated the performance of simpler receptivity models by comparing their receptivity predictions to both the DNS and the experimental results. The receptivity model presented here, which is based on the adjoint PSE, predicts receptivity amplitudes in very good agreement to DNS results. The disturbance amplitudes obtained by Ng & Crouch (1999) who employed FRNT are, on the other hand, more than a factor of 2 higher than the DNS results and thus closely resemble those measured in the experiments. However, as already mentioned by Ng & Crouch (1999), this might be fortuitous since it is well-known that receptivity models based on FRNT overpredict receptivity amplitudes. Considering this, the FRNT predictions by Ng & Crouch (1999) are consistent with our results.

Reasons for the discrepancy between experimental and numerical/theoretical results might be the existence of low-level free-stream turbulence which affects the evolution of steady crossflow vortices or the slight difference between the experimental and numerical pressure coefficients. Also natural roughness upstream of the artificial roughness array could increase the receptivity amplitudes. Our results suggest that such additional effects should be accounted for to correctly model the experimental conditions.

ACKNOWLEDGEMENTS

The authors gratefully acknowledge funding by VR (The Swedish Research Council) and computer time by PDC (Center for High Performance Computing) at KTH Stockholm, Sweden.

REFERENCES

Bertolotti, F. P., Herbert, T. & Spalart, P. R. 1992 Linear and nonlinear stability of the Blasius boundary layer. *J. Fluid Mech.* **242**, 441–474.

Bippes, H. 1999 Basic experiments on transition in three-dimensional boundary layers dominated by crossflow instability. *Progress in Aerospace Sciences* **35**, 363–412.

Eliasson, P. 2002 EDGE, a navier-stokes solver for unstructured grids. In *Proceedings to Finit Volumes for Complex Applications III* (ed. D.Kroner & R. Herbin), pp. 527–534. Hemre Penton Science London.

Fischer, P. F., Lottes, J. W. & Kerkemeier, S. G. 2008 nek5000 Web page. Http://nek5000.mcs.anl.gov.

Haynes, T. S. & Reed, H. L. 2000 Simulation of swept-wing vortices using nonlinear parabolized stability equations. *J. of Fluid Mech.* **405**, 325–349.

Herbert, T. 1997 Parabolized Stability Equations. *Annu. Rev. Fluid Mech.* **29**, 245–283.

Hill, D. C. 1995 Adjoint systems and their role in the receptivity problem for boundary layers. *J. Fluid Mech.* **292**, 183–204.

Hill, D. C. 1997 Receptivity in non-parallel boundary layers. In *Proceedings of the 1997 ASME Fluids Engineering Division Summer Meeting*. ASME.

Maday, Y. & Patera, A. T. 1989 Spectral element methods for the Navier-Stokes equations. In *State of the Art Surveys in Computational Mechanics* (ed. A. K. Noor), pp. 71–143. ASME, New York.

Ng, L. L. & Crouch, J. D. 1999 Roughness-induced receptivity to crossflow vortices on a swept wing. *Phys. Fluids* **11(2)**, 432–438.

Nishino, T. & Shariff, K. 2009 Direct Numerical Simulation of a Swept-Wing Boundary Layer with an Array of Discrete Roughness Elements. In *Proc. 7th IUTAM Symposium on Laminar-Turbulent Transition, Stockholm, Sweden*. Springer.

Nishino, T. & Shariff, K. 2010 Personal communication.

Patera, A. T. 1984 A Spectral Element Method for Fluid Dynamics: Laminar Flow in a Channel Expansion. *J. Comp. Phys.* **54**, 468–488.

Reibert, M. S., Saric, W. S., Carillo, R. B. & Chapman, K. L. 1996 Experiments in nonlinear saturation of stationary crossflow vortices in a swept-wing boundary layer. *AIAA Paper 96-0184* .

Sakov, P. 2011 gridgen-c - an orthogonal grid generator based on the crdt algorithm (by conformal mapping). http://code.google.com/p/gridgen-c/.

Saric, W. S., Jr., R. B. Carillo & Reibert, M. S. 1998 Leading-Edge Roughness as a Transition Control Mechanism. *AIAA Paper 98-0781* .

Schrader, L. U. 2010 Receptivity of boundary layer flows over flat and curved walls. PhD thesis, KTH Stockholm.

Somers, D. M. & Horstmann, K.-H. 1985 Design of a medium-speed, natural laminar-flow airfoil for commuter aircraft applications. *DLR-IB* **129- 85/26**.

Tempelmann, D., Hanifi, A. & Henningson, D. S. 2010 Spatial optimal growth in three-dimensional boundary layers. *J. Fluid Mech.* **646**, 5–37.

Tufo, H. M. & Fischer, P. F. 2001 Fast Parallel Direct Solvers for Coarse Grid Problems. *J. Parallel Distrib. Comput.* **61 (2)**, 151–177.